

Separatrix ion to electron temperature ratio in the TCV and ASDEX Upgrade tokamaks

M. Cavedon¹, D. Brida², F. Bagnato³, R. A. Coosemans⁴, H. Reimerdes⁴, P. Cano-Megias^{2,5}, R. Dux², T. Eich⁶, O. Février⁴, L. Frassinetti⁷, G. Grenfell², G. Harrer⁸, L. Scotti¹, B. Vincent⁴, the ASDEX Upgrade Team[‡], the TCV Team[§], and the EUROfusion Tokamak Exploitation Team^{||}

¹Dept. of Physics “G. Occhialini”, University of Milan-Bicocca, Milan, Italy

²Max Planck Institute for Plasma Physics, Garching, Germany

³ITER Organization, Route de Vinon-sur-Verdon, CS 90 046, 13067 St. Paul Lez Durance Cedex, France

⁴École Polytechnique Fédérale de Lausanne (EPFL), Swiss Plasma Center (SPC), Lausanne, Switzerland

⁵University of Seville, Seville, Spain

⁶Commonwealth Fusion Systems, Cambridge, United States of America

⁷Fusion Plasma Physics, ECSS, KTH Royal Institute of Technology, Stockholm, Sweden

⁸Institute of Applied Physics, Vienna University of Technology, Vienna, Austria

E-mail: marco.cavedon@unimib.it

Abstract. Increased focus has been recently given to the ion temperature T_i near the separatrix and in the Scrape-Off Layer (SOL) due to its impact on plasma confinement, wall sputtering, heat fluxes, and edge turbulence. In current tokamaks, high pedestal collisionality often clamps pedestal top ion and electron temperatures together. However, thermal decoupling occurs in the SOL due to the different ion and electron masses, leading to $T_i/T_e > 1$ at the separatrix and in the SOL.

Despite consistently observing elevated T_i relative to T_e near the separatrix in various tokamaks, a comprehensive study remains missing due to the measurement complexity. This study, for the first time, explores the primary dependencies of T_i/T_e at the separatrix, focusing on the variation of electron density and connection length to scan SOL collisionalities, and the variation of input power to scan ion and electron heat fluxes, in the ASDEX Upgrade and TCV tokamaks. Surprisingly, T_i/T_e shows weak or no dependence on electron density and connection length, despite their expected role in the SOL coupling. However, the T_i/T_e ratio is strongly influenced by ion and electron heating levels in the plasma core. This suggests that the upstream T_i/T_e is primarily regulated by relative ion and electron heat fluxes from the core, with coupling playing a minor role.

[‡] See author list of H. Zohm et al, 2024 Nucl. Fusion 64 112001

[§] See author list of B.P. Duval et al 2024 Nucl. Fusion 64 112023.

^{||} See author list of E. Joffrin et al 2024 Nucl. Fusion 64 112019

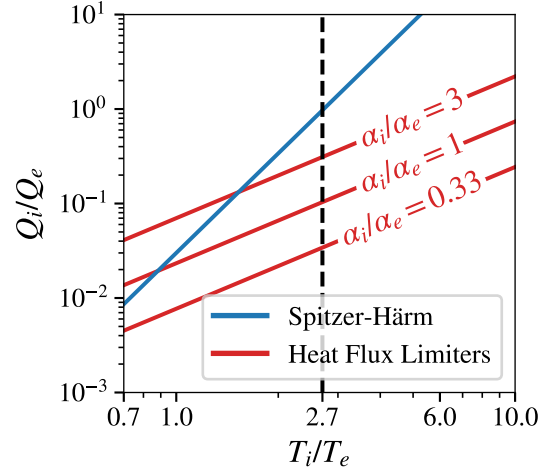


Figure 1. Relation between the integrated ion-to-electron heat flux ratio across the separatrix (Q_i/Q_e) and the upstream ion-to-electron temperature ratio (T_i/T_e), shown for the Spitzer-Härm limit in blue and at three different heat flux limiter ratios in red (adapted from [6]).

Submitted to: *Nucl. Fusion*

1. Introduction

Recently, the importance of the ion temperature T_i close to the separatrix and in the Scrape-Off Layer (SOL) has been given increased attention due to its impact on a range of areas in tokamak physics. This includes determining plasma confinement [1] and understanding plasma-wall interaction processes such as physical sputtering, reflection, and impurity release [2]. Furthermore, the relationship between T_i and the electron temperature T_e is critical in predicting heat fluxes in the SOL [3, 4] and explaining turbulence in the edge region [5]. Therefore, an accurate comprehension of the behavior and dependencies of T_i near the separatrix is essential for setting the conditions and boundaries for various aspects of fusion plasma physics.

In present tokamaks, the pedestal collisionality is generally so high that the pedestal T_i and T_e are clamped together. Nonetheless, in the SOL, the thermal confinement of ions and electrons is short compared to their equilibration time, leading to thermal decoupling. According to the Spitzer-Härm model for heat conduction, the expression for the parallel heat flux of electrons and ions is given by:

$$q_{\text{SH}(e,i)} = \kappa_{0(e,i)} T_{(e,i)}^{5/2} \frac{dT_{(e,i)}}{dl} \quad (1)$$

where $\kappa_{0(e,i)}$ denotes the thermal conductivity for electrons or ions, and l is the coordinate along the field lines. In deuterium plasmas, the thermal conductivity values are approximately $2000 \text{ W eV}^{-7/2} \text{ m}^{-1}$ for electrons and $60 \text{ W eV}^{-7/2} \text{ m}^{-1}$, for ions, as reported in [7]. The difference in thermal conductivity results in ions having a higher

temperature than electrons, a phenomenon consistently supported by measurements [8, 9, 6]. Following the approach of [6], integrating the relation (1) as usual from the upstream region (“u”) to the target (“t”), assuming $T_{u,(e,i)}^{7/2} \gg T_{t,(e,i)}^{7/2}$, and taking the ratio between $T_{u,i}$ and $T_{u,e}$, yields to the following expression:

$$\frac{Q_i}{Q_e} = \frac{\kappa_{0,i}}{\kappa_{0,e}} \left(\frac{T_{u,i}}{T_{u,e}} \right)^{7/2} \quad (2)$$

where Q_i and Q_e are the integrated ion and electron heat flux crossing the separatrix. This relation directly connects the ratio of total ion and electron heat flux to the upstream temperature ratio, as shown in blue in Figure 1. Notably, for $Q_i/Q_e = 1$, Spitzer-Härm predicts $T_i/T_e \approx 2.7$. This suggests that observing a significantly higher T_i compared to T_e upstream is natural and driven by parallel transport in the SOL. However, Spitzer-Härm is a fluid description typically applicable in regimes where power enters the flux tube from the upstream end, while the particle source is concentrated near the target such that convection is negligible, i.e. in the high recycling regime. Such conditions are established at relatively high SOL collisionality, i.e. low temperature and/or high density. However, being a fluid model, Spitzer-Härm implicitly assumes that the electron or ion mean free path is short compared to any other relevant scale length (system or gradient scale lengths). When this assumption breaks down, accounting for kinetic effects becomes necessary. In practise, they are heuristically modeled in codes like SOLPS-ITER [10] or EMC3-EIRENE [11] through a heat flux limiter, an additional term in the parallel heat conduction that is implemented as:

$$q_{\text{FS}(e,i)} = \alpha_{(e,i)} n v_{th(e,i)} k_B T_{(e,i)} \quad (3)$$

where $\alpha_{(e,i)}$ is a heuristic parameter called heat flux limiting factor, and v_{th} the thermal velocity. In fluid codes, the total parallel heat transport is implemented simply as the harmonic average of the Spitzer-Härm and free-streaming heat fluxes and it effectively aims to limit the heat flux a fraction of the free-streaming value ($q_{\text{FS}(e,i)} = n v_{th(e,i)} k_B T_{(e,i)}$). As before, integrating the relation (3) in the SOL, yields to:

$$\frac{Q_i}{Q_e} = \frac{\alpha_i}{\alpha_e} \left(\frac{m_e}{m_i} \right)^{1/2} \left(\frac{T_{u,i}}{T_{u,e}} \right)^{3/2} \quad (4)$$

which again links the ion and electron heat fluxes to the temperature ratios. Note the weaker dependence on the temperature ratio, which allows for a much higher upstream temperature ratio compared to Spitzer-Härm conduction. In the electron case, α_e has been calibrated against SOL kinetic simulations [12] and is typically set to 0.3 [13, 14]. In contrast, α_i remains largely unknown and is often assumed to be equal to α_e . Figure 1 illustrates the relation (4) in red for different values of α_i/α_e , emphasizing the importance of experimentally linking heat fluxes to the temperature ratio. Establishing this connection would be crucial for ensuring the self-consistency of SOL simulations and for cross-validating turbulence codes. This analysis is conducted for the first time in this work, and presented in Section 2.3.

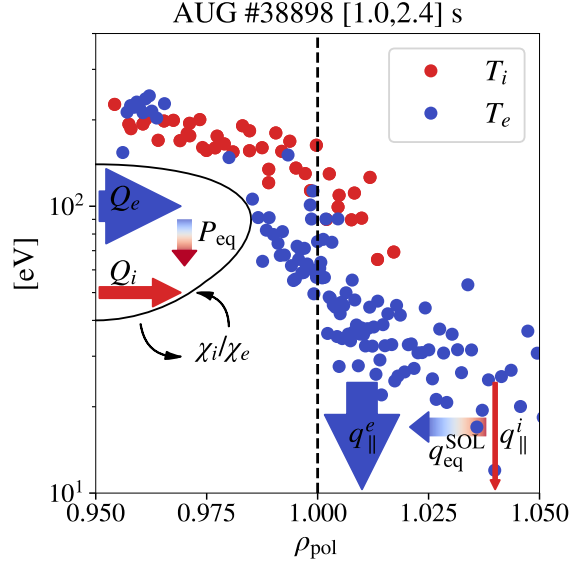


Figure 2. Schematic of the key physics mechanisms regulating the ion (red) to electron (blue) temperature ratio in the vicinity of the separatrix.

All the previous consideration do not include any heat exchange between ion and electrons. While this might seem like an oversight from a core transport perspective, it is important to recall that we are comparing parallel transport, which is obviously much faster than typical perpendicular transport time scales, to equilibration time scales. Stangeby in [7] highlights the importance of heat exchange as being of great importance and propose a model for T_i/T_e , supported by analysis of SOLPS modeling results. As the upstream equipartition between ions and electrons $q_{\text{eq}}^{\text{SOL}}$ is generally much larger than the parallel ion heat flux q_{\parallel}^i , the ion heat is mostly exhausted through the coupling to the electron heat. As a result, the ion to electron temperature ratio scales like the SOL collisionality:

$$\nu_{\text{SOL}} \sim n_{e,u} \cdot \frac{L}{T_i^{5/4} \cdot T_e^{3/4}} \quad (5)$$

where $n_{e,u}$ is the upstream electron density and L the connection length. Moreover, the absolute value of T_i and T_e also depends on the relative strength of the local $q_{\text{eq}}^{\text{SOL}}$ compared to the total perpendicular ion and electron heat flux, Q_i and Q_e respectively, entering in the SOL. Stangeby derived a scaling of the ion to electron temperature ratio based only on JET modelling results obtaining $T_i/T_e \sim ((Q_i/Q_e)/\nu_{\text{SOL}}^*)^{2/7}$. Additionally, the ion-electron coupling plays a role within the confined plasma as well, influencing Q_i and Q_e through the equipartition term P_{eq} , which is calculated as:

$$P_{\text{eq}} \approx \nu_{ie}(T_e - T_i)n_e V \sim \frac{T_e - T_i}{T_e^{3/2}} n_e V \quad (6)$$

where V is the plasma volume and ν_{ie} is the ion-electron collision frequency. Finally, T_i/T_e is influenced also by the ratio of the ion to the electron heat transport, i.e. χ_i/χ_e , which depends on the underlying turbulence and, hence, in turn by T_i/T_e itself [5, 15].

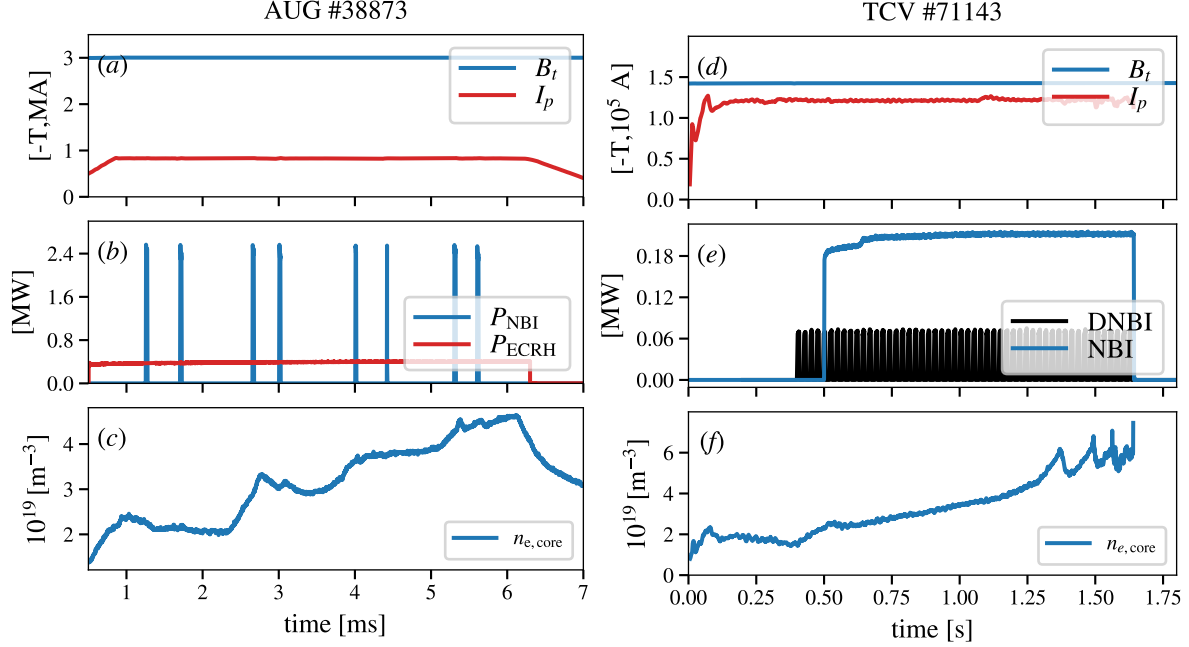


Figure 3. Plasma scenarios in AUG ((a) to (c)) and TCV ((d) to (f)) for studying the ion to the electron temperature ratio at the separatrix. (a),(d): toroidal magnetic field (blue) and plasma current (red); (b),(e) NBI power (blue), ECRH power (red), and diagnostic NBI (black); (c),(f) core line averaged electron density.

This complex feedback mechanism is visually summarized in figure 2, together with some example T_i (red) and T_e (blue) profiles from the ASDEX Upgrade (AUG) tokamak. The reader should note that the assumption made in figure 2 that $Q_e > Q_i$ is for illustration purposes only and does not reflect any general condition.

Although an elevated ion temperature T_i relative to the electron temperature T_e near the separatrix has been consistently observed in various tokamaks, a comprehensive investigation is still lacking due to the complexity of the measurements involved [6, 16]. In this work, we report, for the first time, a study of key dependencies of T_e/T_i at the separatrix, namely n_e , L via magnetic field (B_t) and plasma current (I_p), and input power in the ASDEX Upgrade and TCV tokamak. In particular, to possibly enhance the effect of the ion-electron coupling relative to the total heat fluxes, only L-mode discharges were considered. Along with the absolute temperature values, we also present first calculation of the heat fluxes.

2. Experiments and analysis

The experimental strategy to obtain accurate separatrix T_i/T_e ratios at the ASDEX Upgrade and TCV tokamak in L-mode is different due to the specific characteristics of the two devices and diagnostics involved in this study. In particular, at AUG, the edge and core ion temperature measurements are performed via Charge Exchange Recombination Spectroscopy (CXRS) on an heating beam [17, 18] limiting the possibility

	I_p [MA]	B_t [T]	P_{in} [MW]
AUG	0.8	-2.5, -3.0	Ohmic; ECRH: 0.4
TCV	0.24, 0.28, 0.32	-1.0, -1.2, -1.45	Ohmic; NBI: 0.2; ECRH: 1.3, 3.0, 4.6, 5.0

Table 1. Parameter scan for AUG and TCV

to obtain ion temperature data to only few beam blips as a long phase, typically of the order of 30 ms, of NBI heating would trigger the H-mode. Instead, at the TCV tokamak, the CXRS system is based on a low power (≈ 50 kW), non-perturbing, diagnostic beam [19, 20] (DNBI) allowing continuous measurements during the entire discharge. It is important to note that the traditional charge exchange recombination diagnostic at AUG and TCV does not provide a direct measurement of the temperature of the main ions T_i , but instead measures the temperature of the impurity ions T_Z that are involved in the CX reaction with the beam [21]. Specifically, in the case of the experiments conducted on AUG, the temperature of the fully ionized boron ions was measured, while in the experiments at TCV, the temperature of the carbon ions. Recent advancements in main ion CX systems [22, 23, 24] have shown that T_i is generally lower than T_Z . However, in L-mode—the scenario of interest for this study—the difference at the separatrix remains within the error bars. Notably, a recent study on AUG [25] found no difference between T_i and T_Z at the separatrix. However, depending on the plasma scenario, deviations can occur toward the plasma core, with $T_i > T_Z$. Regarding the electron temperature data, at AUG, the integrated data analysis diagnostic [26] was used, whereas at TCV, the Thomson scattering system [27, 28] was employed. As is traditionally done for determining the separatrix of plasma parameters and their gradients, a linear fit of the logarithmic profiles was performed near the separatrix, typically within a window of $\rho_p \in [-0.98, 1.02]$, to identify the separatrix values of the plasma. The fit was tested with different window sizes and found to be relatively robust, except when using excessively large windows. An exception to this is the T_i data from TCV, for which, as explained later in this section, only data within the separatrix were considered. Furthermore, no radial shifts were applied during profile mapping. It is important to note that this work focuses on the relative changes in T_i/T_e rather than its absolute values. This approach makes the comparison more robust against uncertainties related to equilibrium reconstruction and diagnostic positioning errors.

Figure 3 compares the ASDEX Upgrade (from fig. 3a to fig. 3c) and the TCV (from fig. 3d to fig. 3f) typical discharges used for this study. Figures 3a and 3d show the plasma current I_p in red and toroidal magnetic field B_t in blue. Figures 3b and 3e report the external heating sources: the NBI in blue, the electron cyclotron resonance heating (ECRH) in red, and the DNB in black. Finally, figures 3c and 3f report the core electron density as it is stepped up in AUG and ramped up in TCV. All the discharges analyzed in this work are in the favourable $B \times \nabla B$ configuration in order to have comparable SOL topologies. Moreover, in the case of AUG, the experiments have been performed

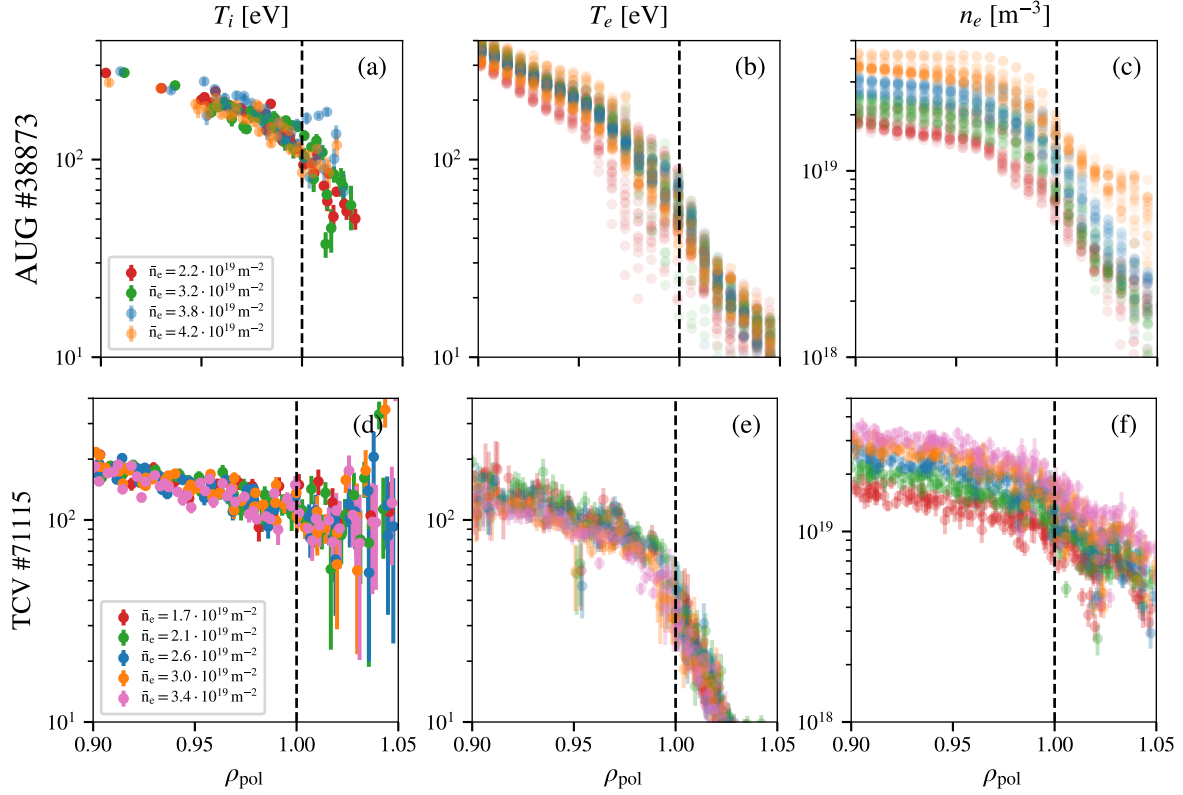


Figure 4. Edge ion temperature ((a), (d)), electron temperature ((b), (e)), and electron density ((c), (f)) for an L-mode density scan in AUG (from (a) to (c)) and TCV (from (d) to (f)). Different colors represent different electron densities.

right after boronization to increase the signal to noise ratio of the CXRS diagnostic. This type of discharge has been performed at different B_t , I_p and input powers for the values reported in Table 1. The ERCH power scan in TCV has been extracted from existing discharges performed at a constant density and is therefore different from the scenario reported in figure 3. In particular, for TCV, accessing the low B_t / high I_p regimes from the possible combinations in Table 1 was not feasible, as it would quickly lead to the β -limit.

2.1. Collisionality scan

The most important parameter to vary in the ν^* scan is the electron density (see equation (5)). Adjusting n_e results in the most significant change in ν^* , reaching up to a factor of two. In contrast, variations in B_t and I_p within the machine limits affect the connection length, leading to changes in ν^* of up to 30%. In figure 4, the edge profiles of T_i (4a), T_e (4b), and n_e (4c) are shown for the AUG discharge depicted in figure 3. Different colors indicate different time points along the discharge. The most striking aspect of this scan is that, despite a roughly twofold increase in the separatrix density, both electron and ion temperatures remain unchanged, resulting in a constant T_i/T_e . This is in clear contrast with Stangeby's model for T_i/T_e at the separatrix. It is important to note that the

range of ν^* scanned in this discharge corresponds exactly to the regime where Stangeby reports a strong dependence of T_i/T_e on ν^* , specifically from approximately $\nu^* = 5 \times 10^{16}$ to $\nu^* = 1 \times 10^{17}$ (see Figure 4.20 in [7]). The averaged value of T_i/T_e over the whole scan is 2.4 ± 0.2 , which is typical for AUG. However, as mentioned at the beginning of this section, the relative alignment between diagnostics is not straightforward, and uncertainties in the equilibrium may introduce errors in the estimation of T_i/T_e . What remains robust, since Figures 4a to 4c show a single discharge, is the relative change of T_i/T_e with n_e , which is the primary purpose of this study.

Figures 4d to 4f show the edge profiles of T_i , T_e , and n_e , respectively, for a density scan at TCV, with different colors indicating different core densities. In the case of TCV, the T_i profiles (Figure 4d) exhibit a significant increase in scatter and error bars for $\rho_{\text{pol}} > 1$. This is a typical effect when the signal-to-noise ratio of the CX emission is very low. In such cases, the Gaussian fit still attempts to converge by fitting over the spectral region where the active and passive parts of the line are subtracted—a process that is never perfect. As a result, the fit often converges to a broader Gaussian, leading to an overestimation of the temperature itself. Nevertheless, the profiles appear reliable up to $\rho \approx 1$, i.e., up to the region of interest. Here, consistent with the observations at AUG, no significant change of T_i or T_e is observed with varying n_e by roughly a factor of 2 (Figure 4e). This further suggests that the coupling between ions and electrons may not be the dominant factor in determining the physics of T_i/T_e at the separatrix.

In figure 5, the widest scans of the connection length for both AUG and TCV are shown, completing the collisionality scan (see equation (5)). For AUG (figures 5(a), 5(b), and 5(c)), only the toroidal magnetic field could be varied from -2.5 T to -3.0 T, leading to an increase in the connection length from approximately 62 m to 75 m. This variation in the magnetic field causes a slight change in both T_i (figure 5(a)) and T_e (figure 5(b)), while their ratio remains stable at around 2.4, consistent with the density scan. However, the change in L is relatively small, which may explain why no corresponding variation in T_i/T_e is observed. A similar trend is seen in the TCV L -scan (figures 5(a), 5(b), and 5(c)). In this case, the variation of current results in an increase in L from 17 m to 24 m. Despite this more significant change, T_i/T_e remains around 2.8 with no noticeable effect. This again indicates that ion-electron coupling is unlikely to be the primary factor shaping the behavior of T_i/T_e at the separatrix in AUG and TCV.

Figure 6 summarizes the entire collisionality scan in one figure by showing T_i/T_e as a function of ν_{SOL}^* and $n_e \cdot L / (T_i^{5/4} \cdot T_e^{3/4})$. The plot shows data from AUG in red and from TCV in blue. For both datasets, triangles correspond to the n_e -scan, while circles indicate the I_p - (L -)scan. The dashed black line illustrates the indicative trend of T_i/T_e , as predicted by modelling results shown in Figure 4.20 of [7]. While the error bars on the measurements are large and the collisionality scan covers only a portion of Stangeby's plot, the ratio T_i/T_e at the separatrix does not appear to be affected by collisionality. Hence, the model assuming that the ion heat flux is mostly exhausted through the electrons does not seem to apply in these cases.

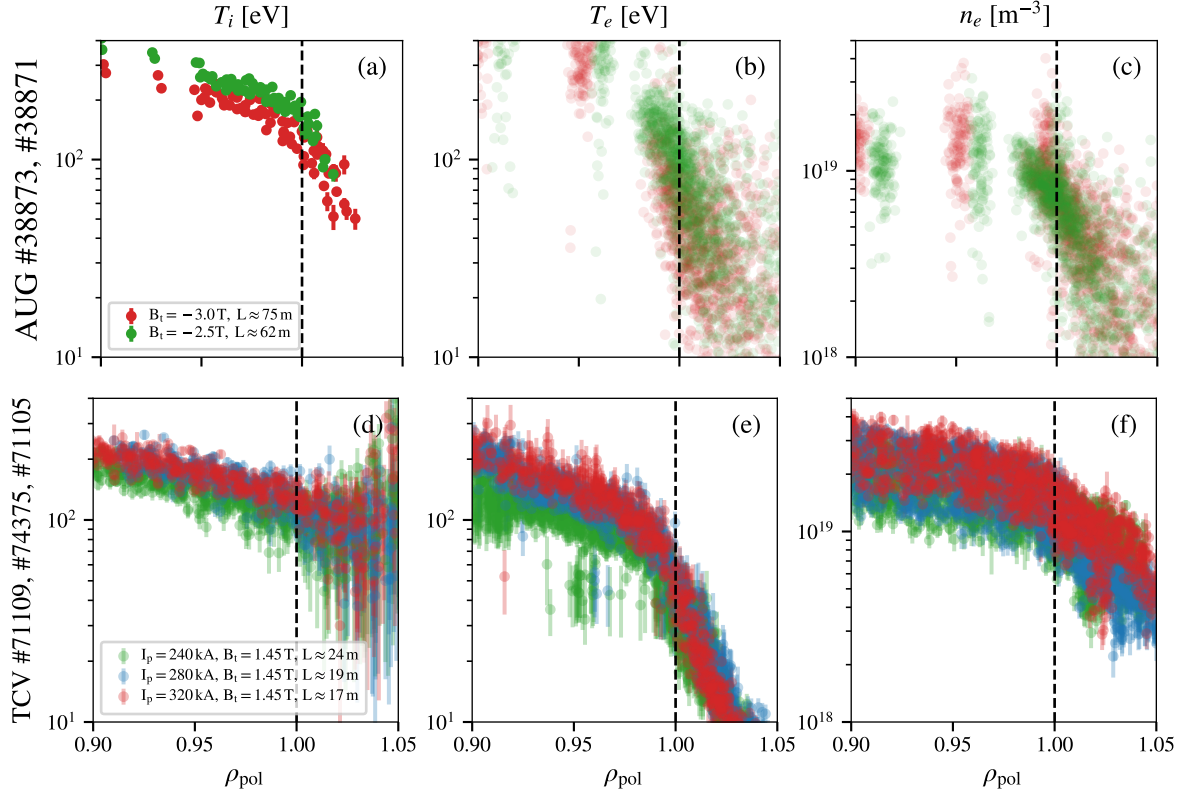


Figure 5. Edge ion temperature ((a), (d)), electron temperature ((b), (e)), and electron density ((c), (f)) for an L-mode connection length scan in AUG (from (a) to (c)) and TCV (from (d) to (f)). Different colors represent different connection lengths.

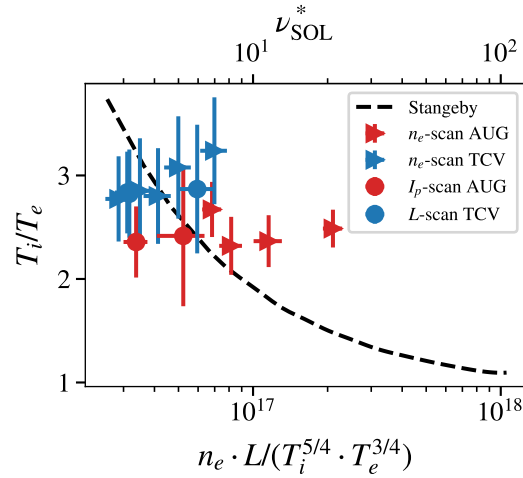


Figure 6. Separatrix ion-to-electron temperature ratio as a function of SOL collisionality. AUG data points are shown in red, with triangles indicating the n_e -scan and circles the I_p -scan. The same symbols are used for TCV data, shown in blue. The dashed black line represents the indicative trend of T_i/T_e from modelling results shown in Figure 4.20 of [7].

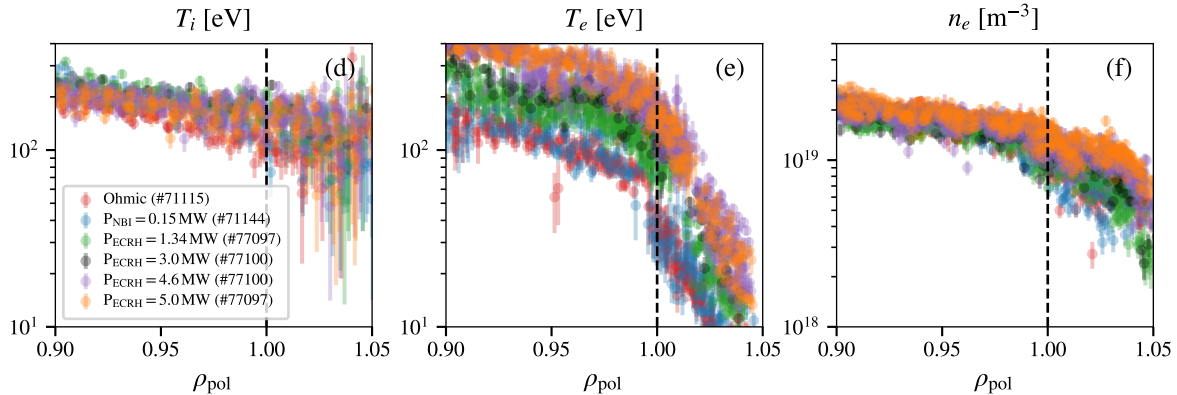


Figure 7. Edge ion temperature (a), electron temperature (d), and electron density (c) for an L-mode power scan in TCV using both NBI and ECRH heating. Different colors represent the different heating methods and power level.

2.2. Power scan

The operational space of ASDEX Upgrade in L-mode with additional heating power is quite limited, as H-mode is triggered very quickly once power is increased. In this experimental study, we could only add 0.4 MW of ECRH, which essentially replaced the ohmic power, as its injection led to a corresponding decrease in ohmic heating. Higher ECRH levels, however, immediately triggered H-mode, making a meaningful comparison with ohmic L-mode discharges impossible. In contrast, TCV allowed for a much wider scan of the heat flux ratio, primarily by adding ECRH in low-density plasmas, where the plasma typically remains in L-mode. The profiles corresponding to increasing ECRH power are extracted from discharges #77097 and #77100. Only one power step was possible with NBI since, as in AUG, higher power would have immediately triggered the L-H transition. The edge profiles from the TCV power scans are shown in figure 7: figure 7(a) shows T_i , figure 7(b) shows T_e , and figure 7(c) shows n_e . The different colors represent the various heating methods and power levels.

Given the increasing electron heating in this power scan, most of the effect is reflected in the electron temperature, while the ion temperature shows relatively small changes. To summarize the effect of the power scan, figure 8 shows the ratio of T_i to T_e as a function of the external input power. Since NBI partially heats the ions and ECRH heats electrons in TCV, the x-axis is ordered with positive values for externally added ECRH power and negative values for NBI power, with zero representing purely ohmic heating. Notably, a substantial amount of electron heating — about 5 MW — is needed to drive T_i/T_e to 1, whereas ohmic heating typically provides only a few hundred kW. This additional electron heating pushes T_i/T_e toward 1, underscoring the importance of Q_i/Q_e as the primary regulator of the separatrix ion-to-electron temperature ratio.

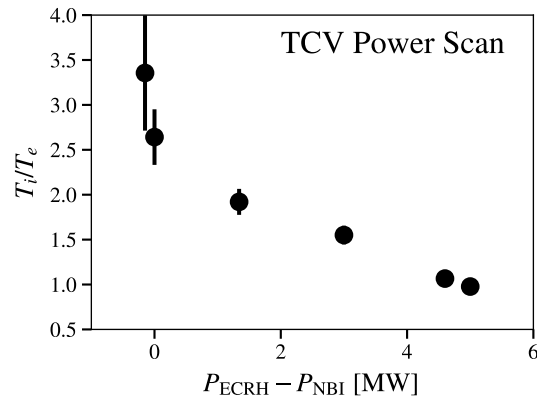


Figure 8. Ion-to-electron temperature ratio for the TCV power scan as a function of the external input power. Since in TCV the NBI partially heats ions and the ECRH heats electrons, the x-axis is arranged with positive values for externally added ECRH power and negative values for NBI power, with zero indicating purely ohmic heating.

2.3. Heat flux limiting factor calculations

Since collisional heat exchange in the SOL between ions and electrons does not seem to play a major role in determining T_i/T_e at the separatrix, the simplified model for parallel heat transport described in the first part of section 1 can be applied. By determining the integrated ion-to-electron heat flux ratio through interpretative transport simulations, e.g. using ASTRA [29] as done in this work, Q_i/Q_e can be plotted as a function of T_i/T_e . This allows for an assessment of whether the experiment hit the heat flux limiter or are at the Spitzer-Härm heat flux levels. Such comparison is most meaningful for the TCV power scan, where Q_i/Q_e and thus T_i/T_e has been varied considerably through the ECRH heating scan. It is important to note that the quantities Q_i and Q_e , provided by ASTRA, represent the total core perpendicular heat flux. However, as discussed in the introduction, what needs to be computed and plotted in Figure 1 is the integrated parallel heat flux. According to [7, 30], this can be calculated as:

$$Q_{\parallel,(i,e)} = \frac{Q_{\perp,(i,e)}}{2\pi R_u \lambda_{T_{(i,e)}} \sin \theta_{\text{pitch},u}} \quad (7)$$

where R_u is the upstream major radius, $\lambda_{T_{(i,e)}}$ is the SOL decay length, and $\sin \theta_{\text{pitch},u}$ is the sine of the upstream pitch angle. When taking the ratio between $Q_{\parallel,i}$ and $Q_{\parallel,e}$, all other terms cancel out, leaving only λ_e/λ_i . This ratio is then used to normalize the ASTRA output.

The results of this analysis are presented in Figure 9. The Spitzer-Härm limit is shown in blue, while three different heat flux limiter ratios, 0.33, 1.0, and 3.0, are plotted in red. Experimental data from the TCV power scan are shown in green, pink, and orange, corresponding to three different values of λ_i/λ_e , namely 1, 2, and 3. It should be noted that a direct experimental determination of λ_i was not possible, as the CXRS data in the TCV scrape-off layer are, as previously mentioned, unreliable. The error bars on Q_i/Q_e indicate the maximum and minimum variations of its value

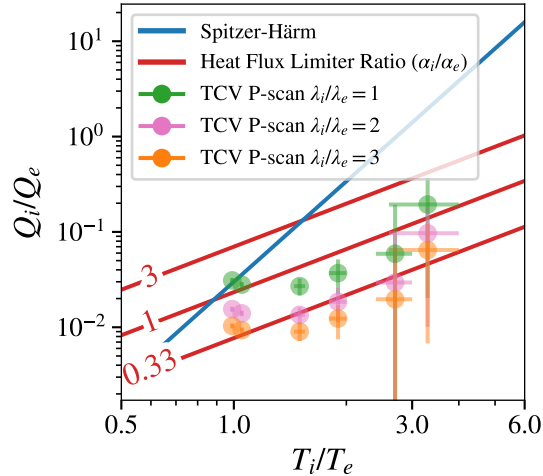


Figure 9. Integrated ion-to-electron heat flux ratio as a function of the separatrix T_i/T_e . The Spitzer-Härm limit is shown in blue, three different heat flux limiter ratios in red, and experimental points from the TCV power scan in green, pink, and orange, corresponding to three different values of λ_i/λ_e , namely 1, 2, and 3.

based on transport simulations using combinations of $T_i \pm \sigma_{T_i}$ and $T_e \pm \sigma_{T_e}$ from the experiments. The points on the right-hand side correspond to those on the left-hand side of Figure 8. As shown in Figure 9, the experimental points align more towards the heat flux limiter limit for an α_i/α_e ratio roughly between 1.0 and 0.3, depending also on λ_i/λ_e . This is roughly consistent with what is assumed in SOL and divertor simulations and marks the first experimental verification of this assumption.

3. Conclusions and Outlook

This study presents a comprehensive investigation into the ion-to-electron temperature ratio (T_i/T_e) at the separatrix in the ASDEX Upgrade and TCV tokamaks. Despite expectations, T_i/T_e showed weak or no dependence on upstream electron density and connection length, suggesting that collisional coupling between ions and electrons in the Scrape-Off Layer (SOL) is not the dominant mechanism regulating T_i/T_e at the separatrix. Instead, the T_i/T_e ratio was found to be primarily influenced by the relative ion and electron heat fluxes from the core, as increased electron heating in TCV through ECRH drove T_i/T_e toward unity. This suggests that core heating balance, not SOL collisionality, is the key factor governing the separatrix temperature ratio. Since collisional coupling is negligible, plotting Q_i/Q_e as a function of T_i/T_e shows that the experimental data align well with the heat flux limiter model for an α_i/α_e ratio between 0.3 and 1.0, consistent with values used in SOL and divertor simulations. This marks the first experimental confirmation of this result.

To build on these findings, dedicated fluid simulations with EMC3-EIRENE are currently underway to reproduce the experimental results and further refine the understanding of the underlying mechanisms regulating the separatrix ion-to-electron

temperature ratio, as for the example the effect of the heat flux limiter. Full-f gyrokinetic simulations would be the next logical step to gain deeper insight into the kinetic part of the parallel transport. In parallel, experiments have already been performed on MAST-U, and data analysis is currently in progress, which will provide an opportunity to test the generality of these results across different tokamak configurations. Moreover, future work will extend this investigation to H-mode plasmas, where the higher confinement and altered edge conditions could reveal new insights into the role of core heating and SOL transport in shaping T_i/T_e .

Acknowledgments

The authors gratefully acknowledge T. Lunt for valuable discussions and insights. This work has been carried out within the framework of the EUROfusion Consortium, partially funded by the European Union via the Euratom Research and Training Programme (Grant Agreement No 101052200 — EUROfusion). The Swiss contribution to this work has been funded by the Swiss State Secretariat for Education, Research and Innovation (SERI). Views and opinions expressed are however those of the author(s) only and do not necessarily reflect those of the European Union, the European Commission or SERI. Neither the European Union nor the European Commission nor SERI can be held responsible for them. This work was supported in part by the Swiss National Science Foundation. This work has received funding from the EUROfusion Consortium (Grant Agreement No CFP-TRED-AWP25-TRED-01).

References

- [1] T. Luda et al. Integrated modeling of ASDEX Upgrade plasmas combining core, pedestal and scrape-off layer physics. *Nuclear Fusion*, 60:036023, 3, February 2020.
- [2] A Kirschner et al. Simulation of the plasma-wall interaction in a tokamak with the Monte Carlo code ERO-TEXTOR. *Nuclear Fusion*, 40:989–1001, 5, May 2000.
- [3] D. Carralero et al. On the role of filaments in perpendicular heat transport at the scrape-off layer. *Nuclear Fusion*, 58:096015, 9, July 2018.
- [4] R.J. Goldston. Heuristic drift-based model of the power scrape-off width in low-gas-puff H-mode tokamaks. *Nuclear Fusion*, 52(1):013009, December 2011.
- [5] P. Manz et al. Physical mechanism behind and access to the I-mode confinement regime in tokamaks. *Nuclear Fusion*, 60:096011, 9, September 2020.
- [6] D. Brunner et al. An assessment of ion temperature measurements in the boundary of the Alcator C-Mod tokamak and implications for ion fluid heat flux limiters. *Plasma Physics and Controlled Fusion*, 55:095010, 9, July 2013.
- [7] P.C Stangeby. The Plasma Boundary of Magnetic Fusion Devices. *The Plasma Boundary of Magnetic Fusion Devices*, January 2000.
- [8] M Kočan et al. Edge ion-to-electron temperature ratio in the Tore Supra tokamak. *Plasma Phys. Control. Fusion*, 50:10, 2008.

- [9] M. Kočan et al. Measurements of ion energies in the tokamak plasma boundary. *Journal of Nuclear Materials*, 415, 1 SUPPL, August 2011.
- [10] S. Wiesen et al. The new SOLPS-ITER code package. *Journal of Nuclear Materials*, 463:480–484, 2015. PLASMA-SURFACE INTERACTIONS 21.
- [11] Y Feng et al. Transport in island divertors: physics, 3D modelling and comparison to first experiments on W7-AS. *Plasma Physics and Controlled Fusion*, 44(5):611, April 2002.
- [12] D. Tskhakaya et al. Kinetic model of the COMPASS tokamak SOL. *Nuclear Materials and Energy*, 26:100893, 2021.
- [13] M. Zhao et al. SOLPS simulations with electron kinetic effects. *Plasma Physics and Controlled Fusion*, 61(2):025019, January 2019.
- [14] A V Chankin et al. SOLPS modelling of ASDEX upgrade H-mode plasma. *Plasma Physics and Controlled Fusion*, 48(6):839, May 2006.
- [15] T. Eich et al. The separatrix operational space of ASDEX Upgrade due to interchange-drift-Alfvén turbulence. *Nuclear Fusion*, 61(8):086017, July 2021.
- [16] S. R. Haskey et al. Main ion and impurity edge profile evolution across the L- to H-mode transition on DIII-D. *Plasma Physics and Controlled Fusion*, 60:105001, 10, August 2018.
- [17] M. Cavedon et al. A fast edge charge exchange recombination spectroscopy system at the ASDEX Upgrade tokamak. *Review of Scientific Instruments*, 88:043103, 4, April 2017.
- [18] R. M. McDermott et al. Extensions to the charge exchange recombination spectroscopy diagnostic suite at ASDEX Upgrade. *Review of Scientific Instruments*, 88:073508, 7, July 2017.
- [19] Alexander N. Karpushov et al. Upgrade of the neutral beam heating system on the TCV tokamak – second high energy neutral beam. *Fusion Engineering and Design*, 187, February 2023.
- [20] F. Bagnato. *Study of impurity ion transport using charge exchange spectroscopy on TCV*, Faculté des sciences de base SPC - Physique du Tokamak TCV, 2022.
- [21] R. J. Fonck et al. Plasma ion temperature measurements via charge exchange recombination radiation. *Applied Physics Letters*, 42(3):239–241, 1983. eprint: <https://doi.org/10.1063/1.93893>.
- [22] B. A. Grierson et al. Active spectroscopic measurements of the bulk deuterium properties in the DIII-D tokamak (invited). *Review of Scientific Instruments*, 83(10):10D529, 2012. eprint: <https://doi.org/10.1063/1.4739239>.
- [23] S. R. Haskey et al. Active spectroscopy measurements of the deuterium temperature, rotation, and density from the core to scrape off layer on the DIII-D tokamak (invited). *Review of Scientific Instruments*, 89(10):10D110, 2018. eprint: <https://doi.org/10.1063/1.5038349>.

- [24] B. Lomanowski et al. Main ion charge exchange spectroscopy on JET in preparation for the DT campaign. In APS Division of Plasma Physics Meeting 2019, editor, 2019.
- [25] P. Cano-Megias et al. Edge deuterium temperature and toroidal velocity at ASDEX Upgrade and comparison to transport models. *to be submitted*, April 2025.
- [26] R. Fischer et al. Integrated Data Analysis of Profile Diagnostics at ASDEX Upgrade. *Fusion Science and Technology*, 58(2):675–684, 2010.
- [27] H. Arnichand et al. New capabilities of the incoherent thomson scattering diagnostics in the tcv tokamak: divertor and real-time measurements. *Journal of Instrumentation*, 14(09):C09013, September 2019.
- [28] P. Blanchard et al. Thomson scattering measurements in the divertor region of the TCV Tokamak plasmas. *Journal of Instrumentation*, 14(10):C10038, October 2019.
- [29] E Fable et al. Novel free-boundary equilibrium and transport solver with theory-based models and its validation against ASDEX Upgrade current ramp scenarios. *Plasma Physics and Controlled Fusion*, 55(12):124028, November 2013.
- [30] T. Lunt et al. Proposal of an alternative upper divertor in asdex upgrade supported by emc3-eirene simulations. *Nuclear Materials and Energy*, 12:1037–1042, 2017. Proceedings of the 22nd International Conference on Plasma Surface Interactions 2016, 22nd PSI.